Terahertz Spectroscopic Investigation of *S*-(+)-Ketamine Hydrochloride and Vibrational Assignment by Density Functional Theory

Patrick M. Hakey, Damian G. Allis, Matthew R. Hudson, Wayne Ouellette, and Timothy M. Korter*

Department of Chemistry, Syracuse University, Syracuse, New York 13244-4100

Received: November 16, 2009; Revised Manuscript Received: January 16, 2010

The terahertz (THz) spectrum of (*S*)-(+)-ketamine hydrochloride has been investigated from 10 to 100 cm^{-1} (0.3−3.0 THz) at both liquid-nitrogen (78 K) and room (294 K) temperatures. Complete solid-state density functional theory structural analyses and normal-mode analyses are performed using a single hybrid density functional (B3LYP) and three generalized gradient approximation density functionals (BLYP, PBE, PW91). An assignment of the eight features present in the well-resolved cryogenic spectrum is provided based upon solid-state predictions at a PW91/6-31G(d,p) level of theory. The simulations predict that a total of 13 infrared-active vibrational modes contribute to the THz spectrum with 26.4% of the spectral intensity originating from external lattice vibrations.

I. Introduction

The analytical applications of terahertz (THz, far-infrared, <200 cm^{-1}) vibrational spectroscopy are based upon the numerous low-energy vibrations found in solid-state compounds and molecules that can be combined to form a spectral "fingerprint." These fingerprints can be used for the identification, detection, and characterization of compounds, including the detection of illicit drugs,[1−3] explosives,[4−6] and, of specific interest within the pharmaceutical realm, the investigation of crystal polymorphs.[7,8] This spectral fingerprint can only be identified reliably if the confidence in the interpretation of the spectrum is very high, indicating that the spectrum originates solely from the compound and/or polymorph of interest and not, for instance, from an uncharacterized polymorph or crystal hydrate of the compound under investigation. The proper interpretation of a solid-state THz spectrum requires an in-depth understanding of the intramolecular (internal) and intermolecular (external) vibrational motions comprising the features present in the experimental spectrum. Assignment of low-energy motions is not yet commonplace in the literature, yet such analyses are crucial to enabling THz spectroscopy to become a more widely accepted analytical technique. Solid-state THz measurements are an example of experimental spectra that can only be assigned accurately through the utilization of solid-state molecular modeling. Density functional theory (DFT) methods provide the most advantageous balance of time and accuracy for accomplishing this.[9−12]

In this study, we present an investigation of (*S*)-(+)-*N*-[1-(2-chlorophenyl)-2-oxocyclohexyl]methanaminium chloride ($C_{13}H_{17}ClNO\cdot Cl$), more generally referred to as (*S*)-(+)-ketamine hydrochloride (*S*-Ket·HCl). The compound is a well-known anesthetic, where its use can create a state of dissociative anesthesia.[13] The enantiomerically pure *S*-Ket·HCl is employed in this study because it is shown to have a potency 4 times that of the *R* enantiomer in terms of pain relief,[14] making it a more likely candidate for long-term abuse. To date, there has been only a small body of work presented to gauge the applicability of THz spectroscopy as a tool for the detection and identification of concealed drugs, with the majority of the available work performed on illicit drugs and not drug precursors or related products.[2,15,16] While two THz investigations have been performed on the racemic form of ketamine hydrochloride,[1,3] no THz studies have been presented on the enantiomerically pure *S*-Ket·HCl.

Experimental THz spectra of *S*-Ket·HCl from 10.0 to 100.0 cm^{-1} (0.3−3.0 THz) at 78 and 294 K, corresponding to liquid-nitrogen temperature and room temperature (RT), are presented in this investigation. A complete first-principles structural analysis of the compound and the assignment of the experimental spectrum utilizing solid-state DFT are also included. A series of solid-state and isolated-molecule calculations are presented to model this ionic molecular solid and enable the assignment of the modes contained within the experimental THz spectrum.

II. Methods

a. Experimental Section. Experimental spectra were recorded using a pulsed time-domain THz spectrometer based upon an amplified Ti:sapphire laser system to generate high-energy femtosecond pulses. Terahertz radiation is generated from these ultrashort pulses via optical rectification,[17,18] and free-space electrooptic sampling (FSEOS) is used to detect the generated THz pulses.[19] Zinc telluride semiconducting crystals (0.5 mm) are used in both the generator and detector components of the instrument. Overall, the system generates THz signals in the range 0.3−3.0 THz and pulse duration of ∼200 fs. A detailed description of the instrument has been provided elsewhere.[9,20]

The sample is held under vacuum in an evacuated variable-temperature cryostat (Janis Research Systems) to allow for temperature studies. The cryostat windows are composed of polymethylpentene (3 mm) due to its low absorbance of THz radiation and high rigidity. During acquisition of the spectral data, the cryostat is held at 294 and 78 K, corresponding to room and liquid-nitrogen temperatures, respectively. The entire path of the THz pulses is purged with dry air to eliminate ambient water vapor.

The sample material, (*S*)-(+)-ketamine hydrochloride, was crushed into a very fine powder by mortar and pestle in order

* Corresponding author. E-mail: tmkorter@syr.edu.

to minimize particle size, thereby decreasing the chance for radiation scattering.[21] After crushing, the sample material was stirred into a poly(tetrafluoroethylene) (PTFE) matrix for its homogeneous dispersion throughout the filler material. The concentration of the sample material in the mixture of PTFE and sample used for the cryogenic experiment was approximately 1.4% by weight. The mixture was then pressed into a pellet with a mass of 0.57 g and 1.8 mm thickness. For the RT experiment, the concentration of *S*-Ket·HCl in PTFE was roughly 2.8% by weight. The pellet formed from this mixture has a mass of 0.58 g and thickness of 1.8 mm. PTFE is utilized as the filler material because it is relatively transparent to radiation in the THz region. THz absorptions have been observed in pure PTFE (and are more noticeable at low temperature),[22,23] but these absorptions can be negated by taking the ratio of the Fourier-transformed power spectrum obtained from the PTFE blank against the Fourier-transformed power spectrum of the sample pellet.

The THz radiation propagating through the sample pellet is averaged a total of 32 times for each individual scan. The averaged data are Fourier-transformed to provide a frequency power spectrum, against which the ratio of the frequency power spectrum created from a PTFE blank is taken. Taking the ratio of the two power spectra results in a THz absorption spectrum containing frequencies in the range 10.0−100.0 cm^{-1} with a full width at half-maximum (FWHM) instrument resolution of ~1.5 cm^{-1}. The room and liquid-nitrogen temperature THz spectra of (*S*)-(+)-ketamine hydrochloride offered in this work are the average of three and four individual absorption spectra, respectively, acquired successively. Use of an averaged spectrum leads to an improved signal-to-noise ratio.

b. Theoretical Section. (*S*)-(+)-Ketamine (*S*-Ket·HCl) solid-state DFT calculations were completed using the CRYSTAL06 software package,[24] and the Gaussian03 software package[25] was used for the study of the protonated isolated molecule (*S*-Ket·H^+). Four density functionals were utilized, including the BLYP,[26,27] PBE,[28,29] and PW91[30] generalized gradient approximation (GGA) density functionals and the B3LYP[26,31] hybrid density functional. A single Gaussian-type basis set, 6-31G(d,p),[32] has been used in conjunction with each of the four density functionals (as the basis sets are the same for all calculations, only the density functional label is used in the Results section). Each of these four combinations was used to optimize the atomic positions within the confines of the unit cell dimensions determined by a single crystal X-ray diffraction study.[33] The optimum sampling of reciprocal space has been determined by monitoring the convergence of the total energy as a function of *K*-point count, with a program-option SHRINK = 7 being used in all CRYSTAL06 calculations presented in this study. Total energy convergence criteria were $\Delta E < 1 \times 10^{-8}$ hartree for geometry optimizations and $\Delta E < 1 \times 10^{-11}$ hartree for normal-mode calculations. CRYSTAL06 calculations utilized an XLGRID [integration grid size: 99, 590]; Gaussian03 calculations employed keyword ULTRAFINE [integration grid size: 99, 590]. This approach has led to the creation of four independent optimized structures and normal-mode analyses at the Γ-point within the harmonic approximation. The crystallographic data determined at 90 K for the monoclinic $P2_1$ crystal are as follows: $a = 8.4338$ (4) Å, $b = 7.0715$ (4) Å, $c = 11.3524$ (6) Å, $\alpha = \gamma = 90.0°$, and $\beta = 101.875°$.[33]

The CRYSTAL06 program is unique in being the only software package currently available utilizing atom-centered basis sets which automates the rigorous calculation of the infrared intensity of each individual vibrational mode in the crystalline state. The IR intensity of each mode is calculated from dipole moment derivatives ($d\mu/dQ$) based on Born atomic charge tensors determined through numerical evaluation of the well-localized Wannier functions of the unit cell.[34,35]

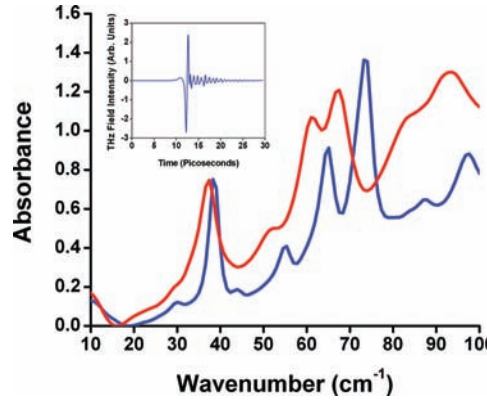

Figure 1. Room-temperature (red) and cryogenic (blue) experimental THz spectra of (*S*)-(+)-ketamine hydrochloride. Included as an inset is the cryogenic THz time-domain waveform of the sample.

TABLE 1: Spectral Absorptions (cm^{-1}) Observed in the Room-Temperature and Cryogenic THz Spectra of (*S*)-(+)-Ketamine Hydrochloride

room temp (294 K)	cryogenic (78 K)
29.5	30.1
37.4	38.3
–	43.9
52.2	55.3
61.1	65.1
67.5	73.3
83.6	87.1
93.5	97.6

III. Results

a. Experimental Section. The room and liquid-nitrogen temperature THz spectra of *S*-Ket·HCl are shown overlaid in Figure 1. The RT spectrum is taken with a pellet having a concentration of 2.8%, while the cryogenic spectrum utilizes a pellet with a lower concentration of 1.4%. The absorbance values increased substantially for the 2.8% sample pellet as the temperature was lowered from RT to liquid-nitrogen temperature; the change in absorbance may be tied to the likely decrease in unit cell dimensions upon cooling. Differing sample concentrations are therefore used to create spectra with similar absorbance values. The two spectra are overlaid in the figure to highlight the correlation between the spectral features observed at both temperatures and to indicate the modest shifts to higher energy visible in the cryogenic spectrum. Table 1 provides the energies of each of the experimentally observed features recorded in the spectra.

A total of seven features are observed in the RT spectrum with a range of spectral intensity. The highest intensity feature occurs in the low-energy portion of the spectrum at 37.4 cm^{-1}. The second and third most intense features are observed at 61.1 and 67.5 cm^{-1}. A fourth moderately intense feature is recorded in the high-energy portion of the spectrum at 93.5 cm^{-1}. The true intensity of this feature is uncertain, but is believed to be more intense than is observed experimentally, as this feature resides quite close to the edge of the maximum bandwidth of the instrument. A weak feature is observed at roughly 52.2 cm^{-1}; the exact position of this feature is difficult to determine because of the weak spectral intensity displayed by this feature. Two

additional features are observed in the RT spectrum, both of which are considered to be shoulder features. A poorly defined shoulder is observed in the low-energy portion of the spectrum at approximately 29.5 cm^{-1}, while a more well-defined shoulder is observed at 83.6 cm^{-1}.

The 78 K spectrum reveals an eighth spectral feature not observed in the RT spectrum and greatly improves the clarity of the spectral features observed in the RT spectrum. This improved clarity is not uncommon and has been seen in earlier work, making cryogenic cooling an invaluable tool for uncovering spectroscopic features and enabling more complete computational assignments of experimental spectra.[36,37] The two spectra can be easily correlated as the features observed in each are quite close in frequency and overall appearance. It appears that the primary difference between the two spectra, other than substantially improved resolution and changes in spectral intensity (consistent with cooling-induced vibrational energy-level population changes), is a moderate shift to higher energy of the features included in the cryogenic spectrum. This shift is typical and is expected based upon decreases in the unit cell dimensions through cooling. In the cryogenic spectrum, a very intense feature is found at 73.3 cm^{-1}, with a second intense feature located at 38.3 cm^{-1}. The third most intense feature is observed at 65.1 cm^{-1}. The fourth highest intensity feature is recorded at 97.6 cm^{-1} at the extreme edge of the instrument bandwidth. As in the case of the RT spectrum, the intensity of this highest energy feature is at a lower level of certainly than the other features because of bandwidth limitations. A moderately intense feature is observed at 55.3 cm^{-1}. The remaining three features all exhibit weak relative intensity and are found at 30.1, 43.9, and 87.1 cm^{-1}. Experimentally measured spectra provided in this investigation are offset vertically to place the minimum absorbance value at zero.

b. Theoretical Section. Calculated structural data for both the solid-state (*S*-Ket·HCl) and protonated isolated-molecule conformations (*S*-Ket·H^+) of (*S*)-(+)-ketamine are included in Tables 2 (bond lengths) and 3 (bond angles). Also included in these tables are the corresponding values determined by the recently published single-crystal diffraction study of the compound.[33] The protonated form of the isolated molecule is the structurally appropriate form of the molecule to use in any computational analysis, as has been described in previous works.[9,11] To enable a quantitative determination of the quality of the bond length and bond angle values predicted by the calculated structures produced from each of the four functionals, root-mean-square-deviation (RMSD) values are provided. The RMSD values for the solid-state and isolated-molecule geometries show the substantial differences in the accuracy between the geometry predictions determined by the solid-state and isolated-molecule methodologies. For ease in identifying the bond lengths and angles being measured, the labeling scheme of the molecule is depicted in Figure 2.

To more easily identify the deviations in the predicted bond lengths from the experimentally observed values, bond length deviation plots for both the solid state and the protonated isolated molecule are provided in Figure 3. This is done to facilitate comparison between the two different methodologies and, unsurprisingly, clearly indicates that the solid-state calculations more accurately predict the actual crystal geometry. The deviations from experiment for both the solid-state and the isolated-molecule calculations are relatively consistent, with both methodologies generally overestimating the diffraction bond lengths. The overestimation is slightly more apparent, in terms of magnitude, in the isolated-molecule predictions. The deviation between the average predicted bond length for the solid state and the isolated molecule is largest in the case of the C_7-N_1 and the C_7-C_8 bonds. In these two cases, the methods deviate by 0.0205 and 0.0202 Å, respectively, with the average distance provided by the isolated-molecule methodology substantially greater than the length predicted by the solid-state calculations. Figure 3 illustrates the rather poor prediction of the C_7-N_1 and C_7-C_8 bond lengths by the isolated-molecule predictions. Also apparent in the figure is the inability of either methodology to accurately predict the Cl_1-C_1 bond length, particularly by the BLYP calculations. In the case of the C_8-C_9 bond, the isolated-molecule calculations *under*estimate the bond length by 0.0025 Å, while the solid-state calculations *over*estimate the length by 0.0086 Å. These values contribute to the fourth largest deviation seen between the two methodologies of 0.0112 Å. The large deviations in the bond lengths predicted by the two methodologies are likely tied to the absence of hydrogen-bonding interactions in the isolated-molecule calculations.

The RMSD values for both the solid-state and the isolated-molecule simulations have been provided in Table 2 to

TABLE 2: Calculated Bond Lengths (Å) and RMSD Values for the Solid-State (*S*-Ket·HCl) and Isolated-Molecule (*S*-Ket·H^+) Calculations [Functional/6-31G(d,p)][a]

Solid State					
bond	exp	B3LYP	BLYP	PBE	PW91
Cl_1-C_1	1.740	1.7574	1.7760	1.7553	1.7560
C_1-C_2	1.384	1.3934	1.4021	1.4006	1.3993
C_2-C_3	1.383	1.3918	1.4012	1.3982	1.3972
C_3-C_4	1.380	1.3929	1.4018	1.3998	1.3987
C_4-C_5	1.387	1.3923	1.4014	1.3988	1.3977
C_5-C_6	1.400	1.4061	1.4161	1.4128	1.4117
C_6-C_1	1.397	1.4071	1.4167	1.4141	1.4127
C_6-C_7	1.532	1.5344	1.5415	1.5335	1.5324
C_7-C_8	1.541	1.5492	1.5610	1.5533	1.5521
C_8-O_1	1.211	1.2188	1.2322	1.2298	1.2289
C_8-C_9	1.502	1.5081	1.5163	1.5094	1.5086
C_9-C_{10}	1.541	1.5486	1.5617	1.5513	1.5510
$C_{10}-C_{11}$	1.526	1.5296	1.5386	1.5300	1.5295
$C_{11}-C_{12}$	1.529	1.5314	1.5406	1.5312	1.5307
$C_{12}-C_7$	1.552	1.5609	1.5728	1.5617	1.5609
C_7-N_1	1.513	1.5191	1.5382	1.5209	1.5204
N_1-C_{13}	1.489	1.4884	1.5008	1.4876	1.4875
RMSD		*0.008*	0.019	0.012	0.012
Isolated Molecule					
bond	exp	B3LYP	BLYP	PBE	PW91
Cl_1-C_1	1.740	1.7668	1.7889	1.7647	1.7656
C_1-C_2	1.384	1.3922	1.4018	1.3988	1.3973
C_2-C_3	1.383	1.3937	1.4039	1.4001	1.3990
C_3-C_4	1.380	1.3931	1.4031	1.3999	1.3987
C_4-C_5	1.387	1.3935	1.4032	1.3996	1.3984
C_5-C_6	1.400	1.4058	1.4174	1.4120	1.4108
C_6-C_1	1.397	1.4105	1.4216	1.4168	1.4153
C_6-C_7	1.532	1.5284	1.5361	1.5256	1.5242
C_7-C_8	1.541	1.5670	1.5854	1.5727	1.5712
C_8-O_1	1.211	1.2180	1.2321	1.2310	1.2301
C_8-C_9	1.502	1.4985	1.5073	1.4966	1.4954
C_9-C_{10}	1.541	1.5553	1.5706	1.5596	1.5592
$C_{10}-C_{11}$	1.526	1.5356	1.5464	1.5362	1.5356
$C_{11}-C_{12}$	1.529	1.5442	1.5562	1.5442	1.5437
$C_{12}-C_7$	1.552	1.5561	1.5688	1.5567	1.5558
C_7-N_1	1.513	1.5393	1.5638	1.5390	1.5387
N_1-C_{13}	1.489	1.4941	1.5077	1.4921	1.4917
RMSD		*0.014*	0.027	0.017	0.017

[a] For the atom labeling scheme, refer to Figure 2. Experimental values (exp) are taken from ref 33.

TABLE 3: Calculated Bond Angles (deg) and RMSD Values for the Solid-State (*S*-Ket·HCl) and Isolated-Molecule (*S*-Ket·H^+) Calculations [Functional/6-31G(d,p)][a]

Solid State					
bond	exp	B3LYP	BLYP	PBE	PW91
$Cl_1-C_1-C_2$	116.23	115.838	115.752	116.086	116.100
$C_1-C_2-C_3$	120.23	120.480	120.389	120.480	120.445
$C_2-C_1-C_6$	122.12	122.006	122.164	121.950	121.989
$C_2-C_3-C_4$	119.15	118.839	118.860	118.879	118.885
$C_3-C_4-C_5$	120.36	120.269	120.283	120.236	120.256
$C_4-C_5-C_6$	121.85	122.269	122.310	122.276	122.242
$C_5-C_6-C_1$	116.28	116.130	115.982	116.172	116.178
$C_6-C_1-Cl_1$	121.64	122.156	122.083	121.964	121.911
$C_5-C_6-C_7$	119.81	119.351	119.475	119.488	119.494
$C_1-C_6-C_7$	123.76	124.320	124.328	124.165	124.166
$C_6-C_7-C_8$	115.60	116.125	116.185	116.073	116.067
$C_7-C_8-O_1$	120.40	120.045	120.190	120.030	120.023
$C_7-C_8-C_9$	114.67	115.093	114.832	114.826	114.846
$O_1-C_8-C_9$	124.15	124.102	124.152	124.338	124.316
$C_8-C_9-C_{10}$	107.63	108.436	108.467	108.501	108.527
$C_9-C_{10}-C_{11}$	110.56	111.207	111.290	111.077	111.040
$C_{10}-C_{11}-C_{12}$	110.96	110.963	110.921	110.695	110.709
$C_{11}-C_{12}-C_7$	111.89	112.099	112.003	111.970	111.957
$C_{12}-C_7-C_8$	103.11	103.245	103.449	103.304	103.340
$C_6-C_7-C_{12}$	113.56	113.437	113.504	113.205	113.143
$N_1-C_7-C_8$	106.18	105.782	105.745	105.751	105.750
$N_1-C_7-C_{12}$	108.52	108.096	107.918	108.021	107.999
$N_1-C_7-C_6$	109.38	109.567	109.439	109.886	109.941
$C_7-N_1-C_{13}$	116.01	116.527	116.286	116.139	116.096
RMSD		0.401	0.400	*0.371*	0.372
Isolated Molecule					
bond	exp	B3LYP	BLYP	PBE	PW91
$Cl_1-C_1-C_2$	116.23	117.015	116.885	117.445	117.473
$C_1-C_2-C_3$	120.23	119.546	119.454	119.415	119.380
$C_2-C_1-C_6$	122.12	122.329	122.531	122.341	122.374
$C_2-C_3-C_4$	119.15	119.743	119.755	119.857	119.868
$C_3-C_4-C_5$	120.36	120.032	120.061	120.019	120.029
$C_4-C_5-C_6$	121.85	121.909	121.982	121.820	121.791
$C_5-C_6-C_1$	116.28	116.422	116.198	116.530	116.540
$C_6-C_1-Cl_1$	121.64	120.645	120.570	120.205	120.143
$C_5-C_6-C_7$	119.81	121.269	121.339	121.551	121.565
$C_1-C_6-C_7$	123.76	122.275	122.436	121.874	121.852
$C_6-C_7-C_8$	115.60	116.908	117.179	117.193	117.166
$C_7-C_8-O_1$	120.40	118.332	118.346	117.987	117.939
$C_7-C_8-C_9$	114.67	115.316	115.256	115.280	115.313
$O_1-C_8-C_9$	124.15	124.843	124.751	125.025	125.025
$C_8-C_9-C_{10}$	107.63	105.821	105.864	105.423	105.391
$C_9-C_{10}-C_{11}$	110.56	111.492	111.541	111.485	111.489
$C_{10}-C_{11}-C_{12}$	110.96	112.726	112.767	112.551	112.547
$C_{11}-C_{12}-C_7$	111.89	112.061	112.031	111.578	111.539
$C_{12}-C_7-C_8$	103.11	102.106	102.063	101.757	101.810
$C_6-C_7-C_{12}$	113.56	115.282	115.489	115.157	115.132
$N_1-C_7-C_8$	106.18	103.018	102.384	102.300	102.255
$N_1-C_7-C_{12}$	108.52	110.061	110.123	110.559	110.570
$N_1-C_7-C_6$	109.38	108.652	108.693	108.998	109.030
$C_7-N_1-C_{13}$	116.01	118.632	119.140	118.784	118.739
RMSD		*1.367*	1.497	1.592	1.601

[a] For the atom labeling scheme, refer to Figure 2. Experimental values (exp) are taken from ref 33.

determine the functional most able to accurately replicate the experimental geometry. In the case of the solid-state bond length predictions, the best RMSD value is attained by the B3LYP hybrid density functional. The PBE and PW91 functionals provide the second best RMSD values behind the B3LYP hybrid, with the BLYP providing the worst RMSD value.

The RMSD values for the isolated-molecule bond length predictions are all higher than their corresponding solid-state values. This difference has been noted repeatedly in prior works and is indicative of the obvious limitations of isolated-molecule calculations for predicting solid-state structural properties.[9,10,20,38] By ignoring the intermolecular forces, such as hydrogen bonding and ionic interactions, present in a crystal cell, the isolated-molecule calculations are incapable of accurately reproducing structural changes to molecules as found in the solid. Despite the inherent limitations of the isolated-molecule calculations, the order of quality for the RMSD values is maintained exactly as it is in the solid-state case, with the B3LYP prediction again providing the lowest RMSD value and the PBE and PW91 density functionals again giving the second best RMSD values.

Table 3 provides the RMSD values for both the solid-state and isolated-molecule bond angle predictions. In terms of RMSD values, the quality of the solid-state predictions deviates from the order attained in the bond length predictions. In the solid-state case, the best bond angle replication is provided by the PBE functional, and is very closely followed by the PW91 density functional. BLYP and the B3LYP density functionals provide the third and fourth best reproductions, respectively, of the experimentally determined bond angles.

The isolated-molecule bond angle predictions fall more in line with the bond length predictions, with the B3LYP hybrid functional again offering the lowest RMSD value. The second best RMSD value was attained by the BLYP functional, with the PBE and PW91 functionals providing the third and fourth ranked values, respectively.

The solid-state predictions are shown to be substantially better than the isolated-molecule calculations, especially in the prediction of the molecular bond angles. The RMSD values for the bond lengths predicted by the solid-state calculations are an average of 31.5% better than the average RMSD values predicted by the isolated-molecule bond length predictions. The average RMSD value for the solid-state bond angle predictions is notably smaller than the average RMSD value provided by the isolated-molecule calculations. The values attained by the solid-state predictions are an average of 74.5% improved over those values predicted by the isolated-molecule predictions. This significant decrease in the RMSD value indicates an important improvement in structural reproduction by moving to the solid-state calculations for the bond angle measurements. The decrease in the RMSD value for the bond length predictions provided by the solid-state reproductions is not as large as the decrease observed for the bond angles; however, a greater than 30% decrease in the RMSD value still indicates a clear improvement when compared to the isolated-molecule structural predictions.

Overall, the solid-state structural reproductions display great improvement over the isolated-molecule simulations. The improvement in quality for the solid state is substantial in terms of both bond length and bond angle reproductions; improvement occurs for all four density functionals. This superiority in structural reproduction is clearly tied to the inclusion of crystal packing interactions that are only present in the solid-state calculations. In the case of *S*-Ket·HCl, the importance of the use of solid-state calculations for the proper comparison with experiment is made even more significant by the presence of an intramolecular hydrogen bond predicted in the isolated-molecule calculation and the resulting change to the NH_2^+ environment in the solid state when the predicted intramolecular $NH_2^+\cdots Cl$ interaction is broken in favor of the formation of an ionic intermolecular $N-H^+\cdots Cl^-$ interaction in the solid. This local geometry change is shown in Figure 4 with the relevant atoms labeled and is summarized below. In the isolated-molecule calculation, hydrogen bonds are formed with both

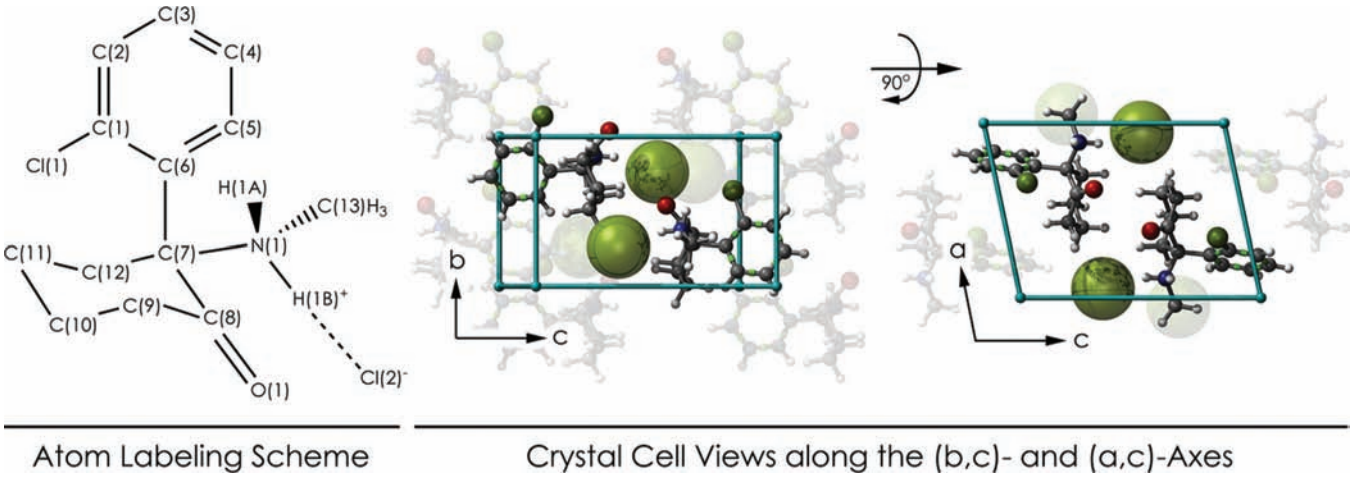

Figure 2. Labeled protonated (*S*)-(+)-ketamine molecule and its nearest anion and two views of the compound in its crystalline packing arrangement. Figure rendered with NanoEngineer-1[43] and POV-Ray.[44]

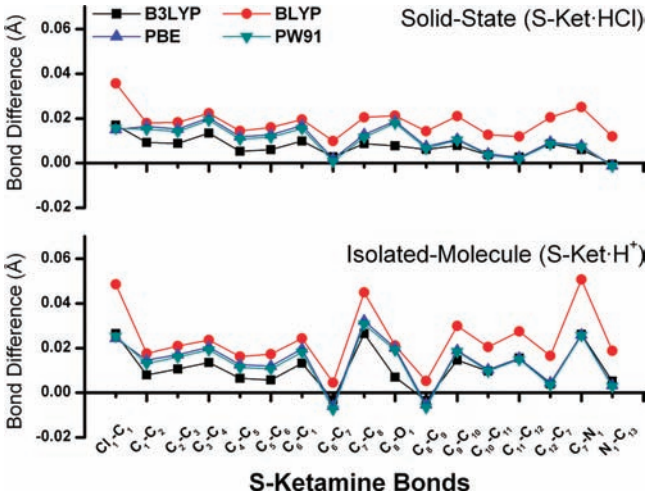

Figure 3. Deviations in calculated bond lengths from experiment for (*S*)-(+)-ketamine. The solid-state deviations are shown on top, while the isolated-molecule deviations are below.

NH_2^+ protons (Cl(1)-**2**) and O (O(1)-**1**). In the solid state, the intramolecular Cl···H^+ hydrogen bonds are broken (Cl(1)a-**2** and Cl(1)b-**4**), O···H hydrogen bonds formed/retained (O(1)a-**2** and O(1)b-**3**), and NH_2^+···Cl^- hydrogen bonds formed (Cl(2)$^-$···**1**,**4**). This local geometry change is discussed with respect to the normal-mode analyses in the following section.

c. Comparison of Simulated and Experimental THz Spectra. Included in Figure 5 is a plot of the four solid-state vibrational simulations plotted against the experimentally observed cryogenic THz spectrum. This image has been created to show the simulation quality attained by each of the spectra generated from the four density functionals. Figure 5 is not of interest simply because of the quality of spectral simulation attained by any one simulation, but for the excellent quality attained from all four simulations. This consistent result is advantageous, as it highlights that multiple functionals can be used effectively to replicate experimental THz measurements, albeit with slightly differing levels of quality. The precise parallel between simulation and experiment in terms of both mode energy and predicted intensity across a series of functionals with the same basis set in this study is in contrast to the results of several prior studies that utilized multiple functionals in the DMol^3 software package[39,40] to simulate experimental THz spectra. The quality of spectral reproduction using CRYSTAL06 observed here is in agreement with a recent study performed on ephedrine,[20] which also utilized CRYSTAL06. This difference in results between this and previous studies is based both on the theoretical methodologies employed by DMol^3 and CRYSTAL06 and, importantly, on available functionality in the two programs, as is discussed in more detail below.

The four simulations each predict a total of 12 IR-active vibrational modes to occur below 100 cm^{-1} in the experimental range, with a 13th IR-active mode predicted at just over 100 cm^{-1} in all four. In all cases, the vibrational modes predicted by each simulation are calculated to occur at slightly higher energies than the experimental features to which they are readily correlated. This shift appears to be systematic and is clearly present in all four simulations, but does not negatively affect the assignment of the experimental features to specific atomic motions. Table 4 includes the predicted vibrational frequencies for both the solid-state and the protonated isolated-molecule conformations of (*S*)-(+)-ketamine.

In order to determine a best performer in terms of the ability of each simulation to accurately reproduce the experimentally measured cryogenic THz spectrum, a two-part statistical analysis has been performed to provide a measure of a simulation's ability to replicate the overall shape of the experimental spectrum and to reproduce the vibrational frequencies of the observed modes. To determine the ability of each simulation to replicate the shape of the experimental spectrum, a cross-correlation has been performed between each level of theory and experiment. For the cross-correlation analysis, the experimental data have been trimmed to only include the range of energies between 20 and 90 cm^{-1}. The trimming of the data is performed to avoid the two areas of the experimental data considered to be of lower confidence because of instrumental limitations. By performing the cross-correlation, two values are generated to gauge the quality of fit. The first of these is the maximum correlation value, and the second is the "lag" value for the theoretical simulation that is applied in order to provide the maximum correlation value. The lag value corresponds to the linear horizontal shift of the theoretical data sets with respect to the experimental data set in order to maximize the correlation between the two data sets. Included in Table 5 are the maximum correlation values, the corresponding lag values, and RMSD values for the peak frequencies. Based upon maximum correlation values, the PW91 simulation provides the best reproduction of the experimental spectrum. In addition, the PW91 provides the smallest lag value, which further indicates how well that simulation replicates the experimental data. The PBE functional

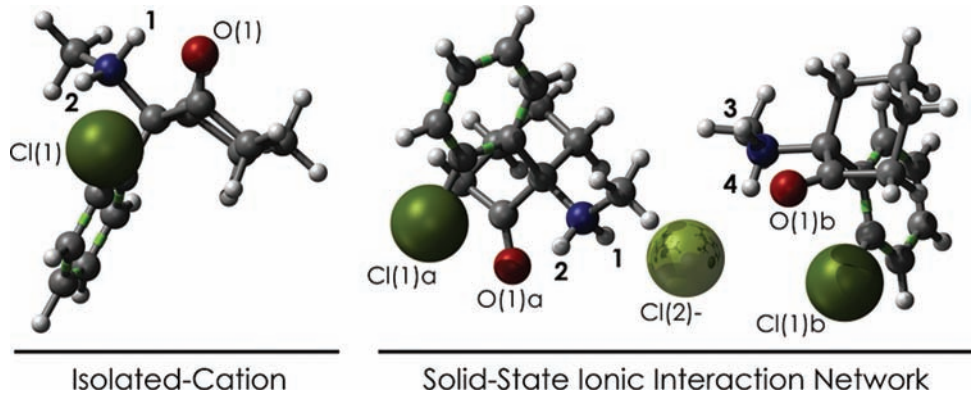

Figure 4. Optimized geometry of *S*-Ket·H^+ (left) and the local ionic environment of *S*-Ket·HCl (right). Figure rendered with NanoEngineer-1[43] and POV-Ray.[44]

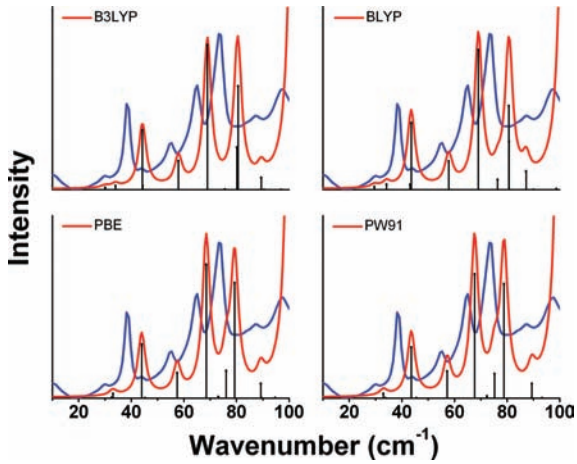

Figure 5. Comparison of the simulated and cryogenic experimental solid-state spectra of (*S*)-(+)-ketamine hydrochloride from 10 to 100 cm^{-1}. The experimental spectrum is provided in blue. The black lines depict the IR intensity of each predicted mode, while the red trace is a convolved plot of the 12 modes occurring in the experimental range using a 3.5 cm^{-1} (FWHM) Lorentzian line shape.

TABLE 4: List of the 13 Lowest-Frequency Normal Modes (cm^{-1}) and Infrared Intensities (km/mol) of Solid-State *S*-Ket·HCl and the Five Lowest-Frequency Normal Modes and Infrared Intensities of *S*-Ket·H^+ [Functional/6-31G(d,p)]

Solid State									
		B3LYP		BLYP		PBE		PW91	
mode	symmetry	freq	int	freq	int	freq	int	freq	int
a	B	34.0	0.25	34.1	0.35	33.1	0.29	33.0	0.30
b	A	30.1	0.14	29.6	0.19	32.5	0.04	33.8	0.02
c	A	44.2	3.92	43.6	4.39	43.9	3.53	43.6	3.34
d	B	44.4	0.25	43.1	0.33	45.2	0.01	45.6	0.01
e	A	57.9	1.90	57.8	1.87	57.5	1.66	57.2	1.78
f	B	68.9	9.51	69.1	9.19	68.5	8.79	67.6	8.16
g	A	75.6	0.03	76.4	0.66	73.1	0.10	72.3	0.13
h	B	80.1	2.78	80.8	3.16	76.1	1.80	75.2	1.60
i	A	80.6	6.80	80.7	5.51	79.3	7.58	78.8	7.51
j	A	90.5	0.00	90.1	0.00	89.5	0.01	89.2	0.00
k	B	89.4	0.79	87.2	1.22	89.2	0.96	89.4	0.96
l	A	97.0	0.00	98.8	0.06	94.7	0.03	93.3	0.02
m	B	101.9	33.80	102.0	31.90	100.7	28.90	100.4	27.95

Isolated Molecule								
	B3LYP		BLYP		PBE		PW91	
mode	freq	int	freq	int	freq	int	freq	int
1	46.4	0.7	44.4	0.7	45.0	0.70	44.9	0.70
2	69.1	0.6	67.2	0.7	67.7	0.73	67.6	0.75
3	92.1	1.0	89.1	1.3	90.9	1.68	91.0	1.71
4	136.4	2.6	132.6	1.6	133.6	0.96	133.9	0.97
5	143.9	3.6	140.8	3.2	144.4	3.20	144.8	3.22

provides the next highest correlation value, followed by the BLYP simulation. In substantial contrast to the reproduction of the bond lengths, the B3LYP density functional provides the smallest correlation value and the largest lag value. The correlation values range across the four simulations from a peak of 31.2 to a minimum of 26.8, while the lag values range from a minimum of 4.5 cm^{-1} to a maximum of 6.0 cm^{-1}.

In addition to determining a best performer in terms of the replication of the shape of the experimental spectrum, a best fit was also determined for the spectral frequencies. This was performed by assigning a total of seven vibrational modes to six spectral features that are located in close proximity to the calculated vibrations. The spectral features used for the assignment were those located at 38.2, 55.3, 65.1, 73.2, 87.1, and 97.6 cm^{-1}. Two of the seven predicted modes were assigned to the spectral feature located at 73.2 cm^{-1}. These six features comprise the great majority of the spectral intensity observed for this compound, meaning the assignment of these six features enables a reasonable determination of the best-fit spectral simulation. As the predicted modes have been assigned to their likely spectral counterparts, an RMSD value can be obtained for each simulation in terms of the reproduction of vibrational frequencies. The PW91 functional provided the highest correlation value, making it the obvious starting point for assigning predicted modes to the experimental features. The correlated modes predicted by each of the three remaining simulations were then assigned to the same experimental features as those for the PW91 functional. Using this approach, RMSD values were obtained for the predicted modes for each functional. The RMSD values determined by this analysis indicate that the PW91 functional also provides the most accurate reproduction of the vibrational frequencies, as it provides the minimum RMSD value for the predicted frequencies. The RMSD values for the vibrational frequencies follow the same general order for the four simulations as was seen for the correlation and lag values. The PBE simulation again provides the second best value, with the BLYP and B3LYP frequency predictions both providing the third best RMSD values using this statistical analysis. The most important result to come from this analysis is the small range of RMSD values for the density functionals, revealing the great consistency in the fits among all four functionals. The values range from the minimum value of 3.5 for PW91 to the maximum value of 5.1 for both the B3LYP and BLYP calculations. The PBE functional provided a frequency deviation RMSD value of 3.9. An earlier study on the compound

TABLE 5: Statistical Analyses Results of the Quality of the Reproduction of the Experimental THz Spectrum of (*S*)-(+)-Ketamine Hydrochloride Using Various Density Functionals[a]

Cross-Correlation Results				
	B3LYP	BLYP	PBE	PW91
correlation	26.8	28.5	30.3	*31.2*
lag	6.0	5.5	5.0	*4.5*
RMSD's of Assignable Features				
exp	B3LYP	BLYP	PBE	PW91
38.2	44.2	43.6	43.9	43.6
55.3	57.9	57.8	57.5	57.2
65.1	68.9	69.1	68.5	67.6
73.2	80.1	80.8	76.1	75.2
73.2	80.6	80.7	79.3	78.8
87.1	89.4	87.2	89.2	89.4
97.6	101.9	102.0	100.7	100.4
RMSD	5.1	5.1	3.9	*3.5*

[a] Cross-correlation values and lag values (cm^{-1}) are provided as well as RMSD values (cm^{-1}) of the calculated frequencies for seven immediately assignable vibrational modes.

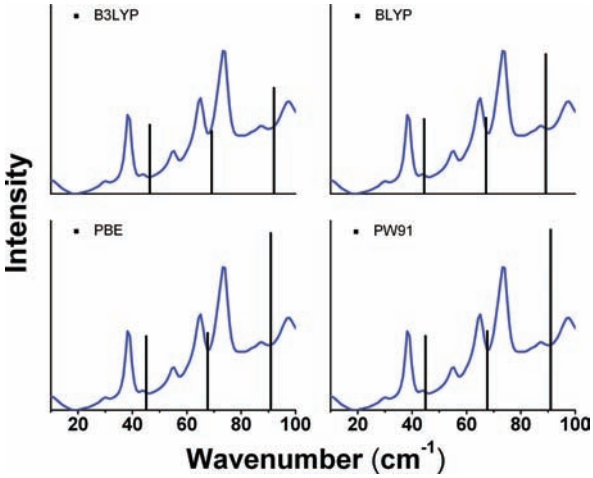

Figure 6. IR intensity of the vibrational modes predicted by the isolated-molecule calculations (black) plotted against the cryogenic experimental spectrum of (*S*)-(+)-ketamine hydrochloride (blue).

ephedrine showed similar results, with the PW91 functional providing a very good reproduction of the experimental THz spectrum.[20]

In order to highlight the inability of the isolated-molecule calculations to properly reproduce experimental solid-state THz spectra, Figure 6 has been included. In this figure, the vibrational frequencies and calculated IR intensities for each of the four isolated-molecule predictions are plotted against the experimental cryogenic spectrum. This image clearly shows the failure of the isolated-molecule calculations as bases for mode assignments, as each of the calculations predicts only three modes to occur in the experimentally observed range where there are at least eight spectral features.

d. THz Mode Assignments from the PW91/6-31G(d,p) Simulation. As the PW91/6-31G(d,p) spectral reproduction provided the best correlation to the experimental spectrum and provided the best reproduction of the spectral frequencies, it was used for the assignment and description of the vibrational modes that comprise the eight features present in the cryogenic experimental spectrum. The isolated-molecule calculation is also used to more easily identify the origins of the intramolecular vibrations present in the solid-state vibrational calculations.

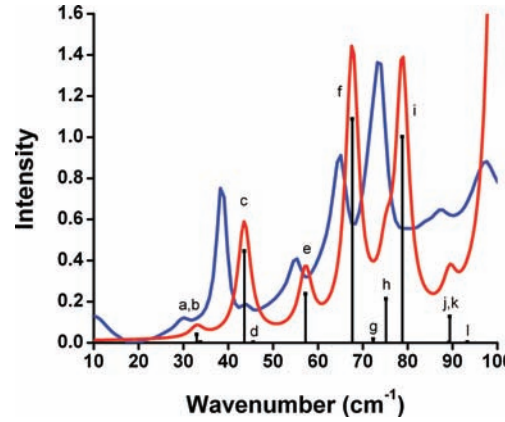

Figure 7. Comparison of the PW91/6-31G(d,p) solid-state simulation to the cryogenic experimental spectrum of (*S*)-(+)-ketamine hydrochloride, shown in blue. The IR intensity for each PW91/6-31G(d,p) mode is shown as a black line. The red trace is a convolved plot of the 12 predicted modes utilizing a 3.5 cm^{-1} (FWHM) Lorentzian line shape. Descriptions for each of the labeled modes are provided in Table 6.

A crystal unit cell which contains M molecules with N atoms includes $3N - 6M$ internal modes (modes pertaining to intramolecular motions), $6M - 3$ external modes (modes correlated to relative motions between the M molecules, i.e., rotations and translations), and three acoustic modes. The crystal cell of *S*-Ket·HCl contains two molecules ($Z = 2$), with each asymmetric unit containing 34 atoms. There are 90 internal modes and nine external vibrational modes present in *S*-Ket·HCl. The nine external modes consist of three optical translational modes and six optical rotational modes.

The assignment of the 12 IR-active vibrational modes that comprise the experimental spectrum is based upon the primary contributor to the vibrational character of each mode. Primary contributions are qualitatively determined through visual inspection of the normal mode displacement eigenvectors. This primary-contributor approach is used because some modes exhibit motions that are composed of both internal and external components, although often one motion clearly dominates the motion description. Generally, the modes predicted in this range can be labeled as either internal or external. External, or intermolecular, modes include motions such as molecular translations, during which the molecule is shifting position and therefore displacing its center of mass, and rotations, during which the entire molecule is rotating about an axis while maintaining the position of the center of mass. During the course of all pure external motions, the atom−atom distances within the molecule are preserved and the motion is defined with respect to a frame of reference beyond the molecule (the unit cell contents in this application). Internal, or intramolecular, modes are strictly defined as being completely represented in terms of a single molecule where the atom−atom distances are the key indicator and, in the THz region, can include such motions as ring twisting, methyl torsions, and molecular bending. The vibrational modes occurring in the experimental range (10−100 cm^{-1}) are labeled "a" through "l". These 12 modes are labeled in Figure 7, in which the PW91 simulation is plotted against the experimental THz spectrum. A 13th mode is predicted at slightly higher than 100 cm^{-1} by the PW91 simulation and is labeled mode "m"; this mode is not included in Figure 7 because it is predicted to occur slightly outside the experimental range. However, mode m is included in Table 6,

TABLE 6: Vibrational Mode Descriptions of *S*-Ket·HCl at the PW91/6-31G(d,p) Level of Theory[a]

freq (cm^{-1})	int (km/mol)	description: solid-state cell contents	molecular mode	% of total intensity
33.0	0.30	IP rotation around crystal *a* axis		0.58
33.8	0.03	IP rotation around crystal *b* axis		0.06
43.6	3.34	OOP rotation around crystal *a* axis + IP Cl^- translation along crystal *b* axis		6.45
45.6	0.01	IP N1−C7 torsion without methyl rotation (twisting of $N-H^+\cdots Cl^-\cdots {}^+H$ network)		0.02
57.2	1.78	OOP rotation around crystal *c* axis		3.44
67.6	8.16	OOP rotation around crystal *b* axis		15.76
72.3	0.13	OOP phenyl torsions and OT along crystal *c* axis	67.6	0.25
75.2	1.60	IP C7−C6 torsion, involving predominantly phenyl rotation only	44.9	3.09
78.8	7.51	OOP C7−C6 torsion in crystal *c* axis; phenyl ring remains stationary while the cyclohexyl ring rotates	44.9	14.50
89.2	0.00	OOP Cl^- translation along the crystal *a* axis + OOP molecule rotation around the crystal *b* axis		0.00
89.4	0.96	IP C7−C6 torsion + Cl^- translation along crystal *b* axis	44.9	1.85
93.3	0.02	IP rotation along crystal *b* axis		0.04
100.4	27.95	IP Cl^- translation along the crystal *a* axis + internal phenyl−Cl wagging motion	67.6	53.97

freq (cm^{-1})	int (km/mol)	description: isolated molecule
44.9	0.70	C7−C6 torsion, twisting of phenyl group with elongation of the intramolecular Cl···H hydrogen bond
67.6	0.75	N1−C7 torsion + OOP phenyl wagging (O···H hydrogen bond is unchanged in the motion)
91.0	1.71	N1−C7 torsion + IP phenyl wagging (resulting in O···H hydrogen bond stretching)
133.9	0.97	cyclohexyl torsional motion and phenyl OOP bending (IP *scissor* motion with Cl···H−N−H···O symmetric stretching)
144.8	3.22	Cyclohexyl torsional motion and C7−C6 (phenyl ring) torsion (OOP NH_2 twisting motion of Cl···H−N−H···O symmetric stretches)

[a] IP, in phase; OOP, out of phase; OT, optical translation.

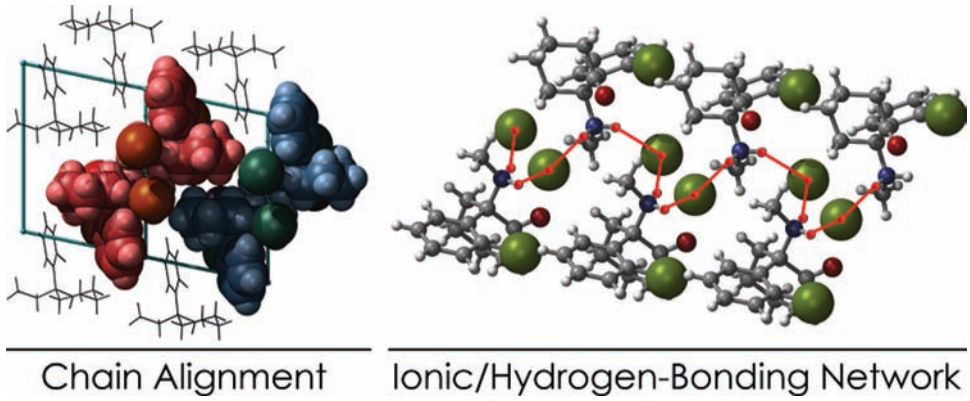

Figure 8. Two molecular chain units (red and blue) formed from two pairs of *S*-Ket·HCl units between neighboring cells along the crystal *a*-axis (left). A view of the network connections between the chain repeat units of each cell is also provided (right). Figure rendered with NanoEngineer-1[43] and POV-Ray.[44]

which includes the names and descriptions of all 13 of these predicted modes.

The division between "solid-state" and "individual chain" mode motions incorporated into Tables 6 and 7 is a result of the difference between the motions of the "in-cell" unit cell contents and the "apparent" object, this object being an ionic/hydrogen-bonding chain that occurs between unit cells. This chain arrangement is shown in Figure 8, with two chains (red and blue) shown for their packing arrangement and one chain (red) shown between two neighboring cells along the crystal *a*-axis (for reference, see Figure 2). The mode motion assignments, otherwise quite complicated using only the in-cell contents of the unit cell, are easily assigned as torsion, translational, or breathing modes (a result of stretching motions in the ionic/hydrogen-bonding network) of the chains when the chain is used as the basis for assignment. As the Γ-point calculation includes half of two neighboring chains, the relative motions of two neighboring chains (the in- and out-of-phase combinations of rotations or chain breathing modes) are not observed in the calculation, meaning the translationally related fragments of the red and blue chains in Figure 8 undergo identical motions within the dipole approximation. The vibrational mode descriptions in terms of chain motion are provided in Table 7. The numerical information provided in Table 7 is identical to that of Table 6, with the only difference between the two being the description of the molecular motions in terms of in-cell (Table 6) versus molecular chain (Table 7) representations of these motions.

TABLE 7: Vibrational Mode Descriptions of *S*-Ket·HCl at the PW91/6-31G(d,p) Level of Theory in Terms of Molecular Chain Motions[a,b]

freq (cm^{-1})	int (km/mol)	individual chain description	molecular mode	% of total intensity
33.0	0.30	OOP chain torsions along crystal *a* axis		0.58
33.8	0.03	OOP chain stretching along crystal *a* axis		0.06
43.6	3.34	IP chain torsions along crystal *a* axis		6.45
45.6	0.01	IP N1−C7 torsions (constrained by $H_3C-HN-H^+\cdots Cl^-\cdots {}^+H$ network)		0.02
57.2	1.78	OOP chain $N-H^+\cdots Cl^-\cdots {}^+H$ breathing mode in the crystal *b* axis		3.44
67.6	8.16	chain phenyl and cyclohexyl IP rocking motion around the $N-H^+\cdots Cl^-\cdots {}^+H$ network		15.76
72.3	0.13	OOP phenyl torsion and $N-H^+\cdots Cl^-\cdots {}^+H$ chain breathing mode	67.6	0.25
75.2	1.60	IP C7−C6 phenyl torsion with a stationary $N-H^+\cdots Cl^-\cdots {}^+H$ network	44.9	3.09
78.8	7.51	IP $N-H^+\cdots Cl^-\cdots {}^+H$ network translational mode in the crystal *a* axis	44.9	14.50
89.2	0.00	IP $N-H^+\cdots Cl^-\cdots {}^+H$ network breathing mode in the crystal *c* axis		0.00
89.4	0.96	OT of the $N-H^+\cdots Cl^-\cdots {}^+H$ network in the crystal *b* axis	44.9	1.85
93.3	0.02	IP $N-H^+\cdots Cl^-\cdots {}^+H$ network stretching mode in the crystal *c* axis		0.04
100.4	27.95	IP chain phenyl wagging mode	67.6	53.97

[a] See Figure 8 and text for details. [b] IP, in phase; OOP, out of phase; OT, optical translation.

IV. Discussion

Both the RT and cryogenic THz spectra of *S*-Ket·HCl are feature-rich, with seven and eight features contained in each spectrum, respectively. The benefit of the cryogenic spectrum is not simply in the uncovering of the eighth spectral feature, but also for the substantially improved spectral resolution. This additional data set is crucial for the development of improved theoretical methodologies for the assignment, analysis, and interpretation of experimental THz spectra. This study also further reinforces the necessity of solid-state calculations for the accurate assignment of condensed-phase THz spectral measurements. The solid-state calculations predict a total of 12 IR-active vibrational modes in the experimental range. This value is in stark contrast to the value predicted by the series of isolated-molecule calculations, all of which predict only three modes to occur in the experimental range.

The four solid-state simulations all provide high qualities of fit to the experimental spectrum. This result is important, as it shows that multiple functionals can be used to provide reasonably accurate solid-state THz simulations, a result that is clearly beneficial, as certain functionals require dramatically more calculation time than others. For instance, the calculation time required for both the structural optimization and the frequency prediction utilizing the B3LYP hybrid density functional is roughly double the calculation time required for the same calculations using any of the three GGA functionals. Admittedly, the structural bond lengths determined using the hybrid functional were superior to the corresponding GGA values, but this modest improvement is found to not be worth the substantial additional computational time for the simulation of the *S*-Ket·HCl THz spectrum. In an attempt to provide the highest quality theoretical spectra, a larger basis set could be employed in this study at the dramatically increased cost of calculation time. An earlier study utilizing both the 6-31G(d,p) and the 6-311G(d,p)[41] basis sets showed the larger basis set provided definite improvements to the spectral simulations, but also required approximately 2.5 times more computational time than is required by the smaller 6-31G(d,p) basis set.[20]

Deviations from the experimental spectrum are clearly present in the four simulations; however, these deviations are relatively small and are generally consistent across the four functionals. The primary deviation in the theoretical simulations is the overestimation of the vibrational frequencies throughout the experimental range by approximately 5 cm^{-1}. The second and equally obvious deviation between theory and experiment is the feature present at the high-energy edge of the experimental spectrum. This feature is correlated to a predicted mode occurring at ~100 cm^{-1}, which is calculated to be a very intense mode despite the observed spectral intensity being moderate. This deviation is most likely the result of limited spectral bandwidth in the experimental measurement, forcing the mode to appear much less intense than it actually is.

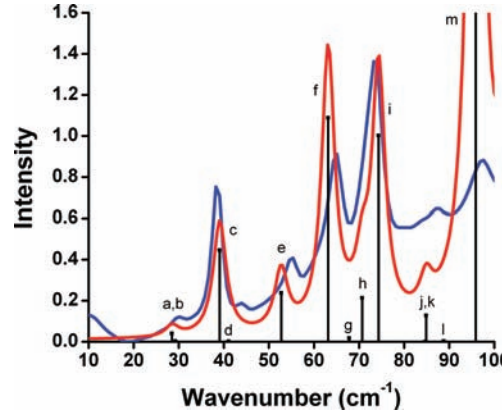

Figure 9. Comparison of the shifted PW91/6-31G(d,p) simulation (red) to the cryogenic experimental spectrum (blue) of (*S*)-(+)-ketamine hydrochloride. The black lines are the predicted IR intensities of the 13 modes included in this range, while the red trace is a convolved plot of the modes utilizing a 3.5 cm^{-1} (FWHM) Lorentzian line shape. The theoretical prediction has been shifted 4.5 cm^{-1} to lower energy to provide the maximum correlation value between the experimental and theoretical data sets.

By utilizing the lag value determined through cross-correlation of the experimental spectrum and the PW91/6-31G(d,p) simulation, Figure 9 has been created. This image has been provided to show the quality of fit possible by shifting the frequencies determined by the theoretical simulation to lower energy by 4.5 cm^{-1}, the lag value determined by cross-correlation to provide the maximum correlation value for this simulation. Modes a−m are labeled on this figure. The physical origin of this shift is unknown, although it is reasonable that this shift is connected to vibrational anharmonicity, as this phenomenon typically decreases normal-mode vibrational frequencies and is unaccounted for in our harmonic-approximation calculations.

The magnitude of the shift is less than the anharmonic corrections reported by other research groups in this spectral region.[42] The structural analysis and the spectral simulation differ in the determination of which functional is most effective. In terms of structural reproduction, the hybrid density functional appears superior to the GGAs utilized in this study. The B3LYP hybrid density functional provides the lowest RMSD value for three of the four categories of structural reproduction, with the solid-state and isolated-molecule bond lengths and the isolated-molecule bond angles all being best reproduced through its use. Solid-state bond angles, however, are best reproduced by the PBE functional.

The results in terms of spectral reproduction are quite opposite the structural results, as all three GGA simulations provide more accurate reproductions of the experimental THz spectrum than the hybrid functional. Among the GGA functionals, the PW91 functional provides the best reproduction in terms of spectral shape and vibrational frequencies.

Based upon the successes of earlier theoretical investigations performed by this research group utilizing the DMol^3 software package,[9−12,38] it was determined that to further investigate the compound with solid-state DFT, a comparable calculation to the PW91/6-31G(d,p) calculation performed with the CRYSTAL06 software package would be completed employing the DMol^3 (version 4.2) software package.[39,40] The DMol^3 calculation utilized the PW91 density functional, but used the DNP (double numerical polarization) basis set,[39] which is comparable to the 6-31G(d,p) Gaussian-type basis set employed by the CRYSTAL06 calculation.

The vibrational frequencies and geometry optimizations provided by DMol^3 certainly have their merits. In the case of *S*-Ket·HCl, the frequencies predicted by each software package differ only by a few wavenumbers, each method calculates the same number of IR-active modes to occur in the experimental range (12), and each predicts a 13th IR-active mode to occur just outside the experimental range (100.4 cm^{-1} for CRYSTAL06 and 102.5 cm^{-1} for DMol^3). The PW91/DNP structural optimization provided by DMol^3 produces better RMSD values for the solid-state bond lengths and bond angles than any of the four geometry optimizations produced using CRYSTAL06 for this compound. When the optimizations using the PW91 functional specifically are compared, the RMSD values for the DMol^3 solid-state bond lengths and bond angles are improved to 0.007 and 0.296, respectively. It is interesting to note that DMol^3 *underestimates* 75% of the studied bond lengths, while CRYSTAL06 *overestimates* 95% of the same bond lengths. While the DMol^3 calculations provide better structural RMSD values, it should be stressed that both it and CRYSTAL06 produce simulations that deviate from experimental measurements by less than 1%, so there is no definitive "poor" performer here. The source of the differences in structural RMSD's is most likely tied to differences in the DNP and 6-31G(d,p) basis sets, with the DNP basis set better tuned for the reproduction of this structure. This quality of agreement between both the theoretical results and the experimental results is made all the more significant by the reduced computational cost of the DMol^3 calculations, which were completed in approximately 1/6 the time of the CRYSTAL06 calculations on comparable hardware.

The comparable predictions of vibrational frequencies and improved structural optimizations provided by DMol^3 for this compound are outweighed by the absence of theoretically rigorous IR intensity calculations in DMol^3 for the reproduction of THz spectra. As has been presented in several previous studies,[10,38] an intensity estimation from the DMol^3 calculations is created based on a difference-dipole method using Mulliken atomic charges to approximate the IR intensity of each predicted vibrational mode. While this approach has yielded reasonable estimates of relative IR intensities for various systems,[10,38] its general utility has been found to be difficult to extend to ionic solids, where the predicted change in atomic charges upon displacement along the normal-mode eigenvectors is found to strongly overestimate some IR intensities.[9,12]

This comparison between two software packages is provided in the interest of addressing only the methodology by which THz researchers can perform solid-state vibrational simulations using DFT programs based on atom-centered basis functions, which itself is based specifically on the previous method surveys and comparisons published by the authors. This is not a point of discussion about theoretical models, but is instead a purely pragmatic statement about how THz researchers must consider the applicability of available software tools to complement their experimental studies. As a general tool for THz spectral property prediction, the inability of DMol^3 to provide rigorously calculated IR intensities greatly reduces its utility compared to CRYSTAL06. That said, DMol^3 is a significantly faster program when the same system is being investigated and is less memory intensive than CRYSTAL06, making it possible to run larger systems on commodity hardware. This resource/performance issue is no different from the purely theoretical balance between larger basis sets and alternate electron correlation methods and the computational demands of running these calculations for the generation of simulations accurate enough to reliably assign experimental spectra. In both cases, developments in hardware and the future development of both programs are expected to change the current state of THz simulations.

V. Conclusions

The THz vibrational spectrum of (*S*)-(+)-ketamine hydrochloride has been investigated from 10 to 100 cm^{-1} at both room and liquid-nitrogen temperatures and has been assigned via solid-state and isolated-molecule DFT calculations. By accounting for intermolecular hydrogen bonding and other crystal packing interactions, the solid-state calculations better reproduce the molecular geometry of the crystal unit cell. Solid-state calculations are also far more effective in the naming and assignment of the experimental spectrum. Vibrational predictions created at the PW91/6-31G(d,p) level of theory are utilized in the assignment of the spectrum, with the solid-state simulation predicting 12 IR-active modes in the experimental range. The prediction of only three IR-active modes in the isolated-molecule calculations for an experimental spectrum containing at least eight features further highlights the inadequacy of isolated-molecule calculations for the assignment of THz spectra. Of the 12 IR-active modes in the solid-state PW91/6-31G(d,p) calculations, eight are external modes that account for 26.4% of the overall spectral intensity.

Acknowledgment. This work was supported by a grant from the National Science Foundation CAREER Program (CHE-0847405). This work was partially supported by the National Center for Supercomputing Applications under [TG-CHE080041N] and utilized the SGI Altix [Cobalt]. P.M.H. would like to express his gratitude to the Syracuse University STEM and GEM Fellowship programs for their continued support. D.G.A. thanks the office of the Vice President for Research at Syracuse University for research support. The authors also acknowledge Dr. John Belote (Syracuse University) for assistance in procuring the research samples.

References and Notes

(1) Wang, G.; Shen, J.; Jia, Y. *J. Appl. Phys.* **2007**, *102*, 013106/1.

(2) Dobroiu, A.; Sasaki, Y.; Shibuya, T.; Otani, C.; Kawase, K. *Proc. IEEE* **2007**, *95*, 1566.
(3) Lu, M.; Shen, J.; Li, N.; Zhang, Y.; Zhang, C.; Liang, L.; Xu, X. *J. Appl. Phys.* **2006**, *100*, 103104/1.
(4) Hu, Y.; Huang, P.; Guo, L.; Wang, X.; Zhang, C. *Phys. Lett. A* **2006**, *359*, 728.
(5) Leahy-Hoppa, M. R.; Fitch, M. J.; Zheng, X.; Hayden, L. M.; Osiander, R. *Chem. Phys. Lett.* **2007**, *434*, 227.
(6) Federici, J. F.; Schulkin, B.; Huang, F.; Gary, D.; Barat, R.; Oliveira, F.; Zimdars, D. *Semicond. Sci. Technol.* **2005**, *20*, S266.
(7) Zeitler, J. A.; Taday, P. F.; Newnham, D. A.; Pepper, M.; Gordon, K. C.; Rades, T. *J. Pharm. Pharmacol.* **2007**, *59*, 209.
(8) Taday, P. F.; Bradley, I. V.; Arnone, D. D.; Pepper, M. *J. Pharm. Sci.* **2003**, *92*, 831.
(9) Hakey, P. M.; Allis, D. G.; Ouellette, W.; Korter, T. M. *J. Phys. Chem. A* **2009**, *113*, 5119.
(10) Allis, D. G.; Korter, T. M. *ChemPhysChem* **2006**, *7*, 2398.
(11) Allis, D. G.; Hakey, P. M.; Korter, T. M. *Chem. Phys. Lett.* **2008**, *463*, 353.
(12) Hakey, P. M.; Hudson, M. R.; Allis, D. G.; Ouellette, W.; Korter, T. M. *J. Phys. Chem. A* **2009**, *113*, 13013.
(13) Domino, E. F.; Chodoff, P.; Corssen, G. *Clin. Pharmacol. Ther.* **1965**, *6*, 279.
(14) Mathisen, L. C.; Skjelbred, P.; Skoglund, L. A.; Oeye, I. *Pain* **1995**, *61*, 215.
(15) Li, N.; Shen, J.; Sun, J.; Liang, L.; Xu, X.; Lu, M.; Yan, J. *Opt. Express* **2005**, *13*, 6750.
(16) Kawase, K.; Ogawa, Y.; Watanabe, Y. *Opt. Express* **2003**, *11*, 2549.
(17) Nahata, A.; Weling, A. S.; Heinz, T. F. *Appl. Phys. Lett.* **1996**, *69*, 2321.
(18) Rice, A.; Jin, Y.; Ma, X. F.; Zhang, X. C.; Bliss, D.; Larkin, J.; Alexander, M. *Appl. Phys. Lett.* **1994**, *64*, 1324.
(19) Wu, Q.; Litz, M.; Zhang, X. C. *Appl. Phys. Lett.* **1996**, *68*, 2924.
(20) Hakey, P. M.; Allis, D. G.; Hudson, M. R.; Ouellette, W.; Korter, T. M. *ChemPhysChem* **2009**, *10*, 2434.
(21) Shen, Y. C.; Taday, P. F.; Pepper, M. *Appl. Phys. Lett.* **2008**, *92*, 051103/1.
(22) Chantry, G. W.; Fleming, J. W.; Nicol, E. A.; Willis, H. A.; Cudby, M. E. A. *Chem. Phys. Lett.* **1972**, *16*, 141.
(23) Johnson, K. W.; Rabolt, J. F. *J. Chem. Phys.* **1973**, *58*, 4536.
(24) Dovesi, R.; Saunders, V. R.; Roetti, C.; Orlando, R.; Zicovich-Wilson, C. M.; Pascales, F.; Civalleri, B.; Doll, K.; Harrison, N. M.; Bush, I. J.; D'Arco, P.; Llunell, M. *CRYSTAL06 User's Manual*; University of Torino: Torino, 2006.
(25) Frisch, M. J. ; Trucks, G. W.; Schlegel, H. B.; Scuseria, G. E.; Robb, M. A.; Cheeseman, J. R.; Montgomery, J. A., Jr.; Vreven, T.; Kudin, K. N.; Burant, J. C.; Millam, J. M.; Iyengar, S. S.; Tomasi, J.; Barone, V.; Mennucci, B.; Cossi, M.; Scalmani, G.; Rega, N.; Petersson, G. A.; Nakatsuji, H.; Hada, M.; Ehara, M.; Toyota, K.; Fukuda, R.; Hasegawa, J.; Ishida, M.; Nakajima, T.; Honda, Y.; Kitao, O.; Nakai, H.; Klene, M.; Li, X.; Knox, J. E.; Hratchian, H. P.; Cross, J. B.; Bakken, V.; Adamo, C.; Jaramillo, J.; Gomperts, R.; Stratmann, R. E.; Yazyev, O.; Austin, A. J.; Cammi, R.; Pomelli, C.; Ochterski, J. W.; Ayala, P. Y.; Morokuma, K.; Voth, G. A.; Salvador, P.; Dannenberg, J. J.; Zakrzewski, V. G.; Dapprich, S.; Daniels, A. D.; Strain, M. C.; Farkas, O.; Malick, D. K.; Rabuck, A. D.; Raghavachari, K.; Foresman, J. B.; Ortiz, J. V.; Cui, Q.; Baboul, A. G.; Clifford, S.; Cioslowski, J.; Stefanov, B. B.; Liu, G.; Liashenko, A.; Piskorz, P.; Komaromi, I.; Martin, R. L.; Fox, D. J.; Keith, T.; Al-Laham, M. A.; Peng, C. Y.; Nanayakkara, A.; Challacombe, M.; Gill, P. M. W.; Johnson, B.; Chen, W.; Wong, M. W.; Gonzalez, C.; Pople., J. A. *Gaussian 03*, revision C.02; Gaussian, Inc.: Wallingford, CT, 2004.
(26) Becke, A. D. *Phys. Rev. A: At., Mol., Opt. Phys.* **1988**, *38*, 3098.
(27) Lee, C.; Yang, W.; Parr, R. G. *Phys. Rev. B: Condens. Matter Mater. Phys.* **1988**, *37*, 785.
(28) Perdew, J. P.; Burke, K.; Ernzerhof, M. *Phys. Rev. Lett.* **1996**, *77*, 3865.
(29) Perdew, J. P.; Burke, K.; Ernzerhof, M. *Phys. Rev. Lett.* **1997**, *78*, 1396.
(30) Perdew, J. P.; Chevary, J. A.; Vosko, S. H.; Jackson, K. A.; Pederson, M. R.; Singh, D. J.; Fiolhais, C. *Phys. Rev. B: Condens. Matter Mater. Phys.* **1992**, *46*, 6671.
(31) Becke, A. D. *J. Chem. Phys.* **1993**, *98*, 5648.
(32) Hariharan, P. C.; Pople, J. A. *Theor. Chim. Acta* 1973*28* 213.
(33) Hakey, P.; Ouellette, W.; Zubieta, J.; Korter, T. *Acta Crystallogr., Sect. E: Struct. Rep. Online* **2008**, *E64*, o1487.
(34) Zicovich-Wilson, C. M.; Dovesi, R.; Saunders, V. R. *J. Chem. Phys.* **2001**, *115*, 9708.
(35) Pascale, F.; Zicovich-Wilson, C. M.; Gejo, F. L.; Civalleri, B.; Orlando, R.; Dovesi, R. *J. Comput. Chem.* **2004**, *25*, 888.
(36) Laman, N.; Harsha, S. S.; Grischkowsky, D.; Melinger, J. S. *Opt. Express* **2008**, *16*, 4094.
(37) Walther, M.; Plochocka, P.; Fischer, B.; Helm, H.; Jepsen, P. U. *Biopolymers* **2002**, *61*, 310.
(38) Allis, D. G.; Prokhorova, D. A.; Korter, T. M. *J. Phys. Chem. A* **2006**, *110*, 1951.
(39) Delley, B. *J. Chem. Phys.* **1990**, *92*, 508.
(40) Delley, B. *J. Chem. Phys.* **2000**, *113*, 7756.
(41) Krishnan, R.; Binkley, J. S.; Seeger, R.; Pople, J. A. *J. Chem. Phys.* **1980**, *72*, 650.
(42) Zhang, H.; Siegrist, K.; Plusquellic, D. F.; Gregurick, S. K. *J. Am. Chem. Soc.* **2008**, *130*, 17846.
(43) *NanoEngineer-1*, 1.1.1 ed.; Nanorex Inc.: Bloomfield Hills, MI.
(44) *POV-Ray*, 3.6 ed.; Persistence of Vision Raytrace Program.

JP910861M